# Supplementary information for

Ultra-broadband polarisation beam splitters and rotators based on 3D-printed waveguides

A. Nesic[1†*], M. Blaicher[1,2†], P. Marin-Palomo[1], C. Füllner[1],
S. Randel[1], W. Freude[1], C. Koos[1,2,3*]

[1]Institute of Photonics and Quantum Electronics (IPQ), Karlsruhe Institute of Technology (KIT), Karlsruhe, Germany. [2]Institute of Microstructure Technology (IMT), Karlsruhe Institute of Technology (KIT), Eggenstein-Leopoldshafen, Germany. [3]Vanguard Automation GmbH, Karlsruhe, Germany. [†]These authors contributed equally to this work. [*]e-mail: aleksandar.nesic@kit.edu; christian.koos@kit.edu

S1. Impact of geometrical variations and combination with protective overcladding

3D-printed waveguides are commonly overclad by additional materials that may serve as a mechanical support and an environmental protection[1]. The presence of such a cladding material, however, might require some design adaptations to compensate the associated changes of the refractive-index contrast. Specifically, embedding the PBS shown in Fig. 2 of the main manuscript into a cladding material with a refractive index $n_{clad} > 1$ would decrease the geometrical birefringence of the partial waveguides WG$_H$ and WG$_V$, which would impair the performance and increase the length L of the Y-branch, see Fig. 2a, such that the overall size of the structure could exceed the write-field size of commonly used two-photon lithography systems. It is therefore favourable to maintain the high index-
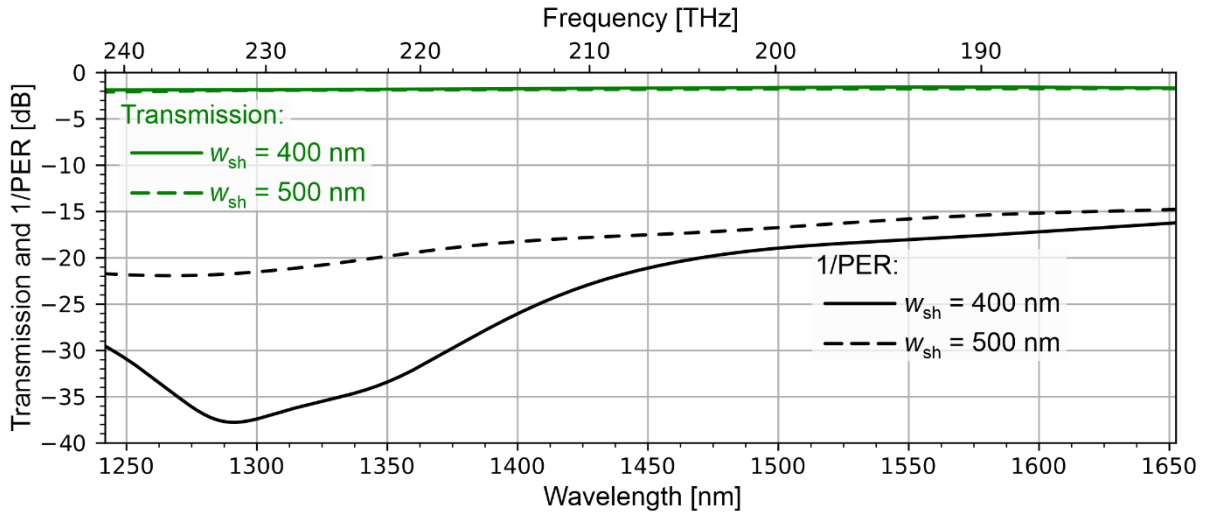

Figure S1: Simulated sensitivity of the transmission $\left|\underline{S}_{E_H^{(H)}E_H^{(I)}}\right|^2 = \left|\underline{S}_{E_V^{(V)}E_V^{(I)}}\right|^2$ **and the polarisation extinction ratio (PER) of the PBS with respect to the smaller dimension w_{sh} of the fabricated partial waveguides WG$_H$ and WG$_V$.** The performance of the PBS strongly depends on the birefringence of these partial waveguides, which in turn depends on the aspect ratio $w_{lo,max}/w_{sh}$, see Fig. 2a of the main manuscript. In case of an increased width w_{sh} of the two partial waveguides from designed 400 nm to 500 nm caused, e.g., by a limited resolution of the underlying 3D-printing system, the PER degrades. Nevertheless, the PER figures are still acceptable and range from 14.8 dB to 21.9 dB within the 410 nm wavelength range. The degradation of the transmission is negligible within the same wavelength range. The PBS design is therefore sufficiently robust with respect to the resolution changes of the 3D-printing system. Note that the design of our structure was not yet optimised for tolerance with respect to fabrication inaccuracies, which might lead to even more robust performance.

contrast at least in the region of the Y-branch, e.g., by means of 3D-printed shielding structures that prevent this region of the structure from getting in direct contact with the cladding material. Such concepts are subject of ongoing research.

It should also be noted that the work presented here relies on a small number of 3D-printed PBS/PR test structures, without any statistical investigations of the robustness of the design in presence of process variations. While the PR is fairly insensitive to smaller geometrical variations, the performance of the PBS crucially relies on the aspect ratio $w_{lo,max}/w_{sh}$ of the cross section of the partial waveguides WG_H and WG_V and might thus be sensitive with respect to geometrical deviations of the fabricated structures from their designed counterparts. Specifically, in case of limited lithographical resolution, the smaller dimension w_{sh} of the fabricated partial waveguides might be bigger than designed, thereby reducing the aspect ratio and hence the associated birefringence. We have investigated this case by repeating the simulation of the S-parameters for partial waveguides having widths w_{sh} of 500 nm instead of the desired 400 nm and by extracting the transmission $\left|\underline{S}_{E_H^{(H)}E_H^{(I)}}\right|^2 = \left|\underline{S}_{E_V^{(V)}E_V^{(I)}}\right|^2$ as well as the PER in analogy to Fig. 2c of the main manuscript. The results are shown as dashed lines in Fig. S1, along with the corresponding parameters for the original structure, indicated by solid lines. At a wavelength of 1550 nm, the transmission decreases only very slightly from −1.55 dB to −1.75 dB while the PER reduces from 18 dB to 15.8 dB. At shorter wavelengths of, e.g., 1300 nm, the degradation of the PER is more pronounced, but the PER at this wavelength is still superior to its counterpart at 1550 nm and exceeds 20 dB. These findings are in good agreement with the measurement and simulation results obtained for the actually fabricated PBS/PR structure, see Section S2. We hence conclude that the proposed 3D-printed PBS/PR structures are sufficiently robust with respect to process variations and that the concept is thus amenable to robust high-volume manufacturing with good reproducibility. In this context, it should also be noted that previous statistical analyses performed on other 3D-printed structures such as simple single-mode waveguides[1] demonstrated the high reproducibility of the underlying structuring technique. Note also that the current design of our structure was not yet optimised for good tolerance with respect to fabrication inaccuracies, which might lead to even more robust performance.

S2. Measurement of polarisation extinction ratio (PER)

We tested our PBS structures by measuring the PER over a broad range of wavelengths. To this end, the polarisation at the input of the structure is varied randomly by a polarisation scrambler, while the Stokes vector and the power at the device output are continuously recorded by a polarimeter, see Fig. S2a for a sketch of the associated setup. The measurement was performed with a commercially available optical component analyser (Keysight N7788B) and was repeated for each of the output ports, thereby revealing the output polarisation state of maximum and minimum transmission as well as the associated PER. The PBS test structure used in this experiment is 3D-printed on the facet of an SMF array which is connected to the polarisation scrambler. At the output, the structure is equipped with a pair of polarisation rotators (PR), realised by rectangular waveguides that are twisted along the propagation direction[2,3]. Twisting one waveguide by +45° and the other by −45°, thus provides identical polarisations at both ports, see Fig. S2b. For better probing of the output, the structure is equipped with adiabatic mode-field adapters that are held by a table-like mechanical support structure, see Fig. 4a of the main manuscript, and that can be individually probed by moving an SMF to the respective port. Note that, due to the unknown polarisation rotation in the SMF, our measurement only allows to determine the exact polarisation state at the input of the polarimeter, but not at the output ports
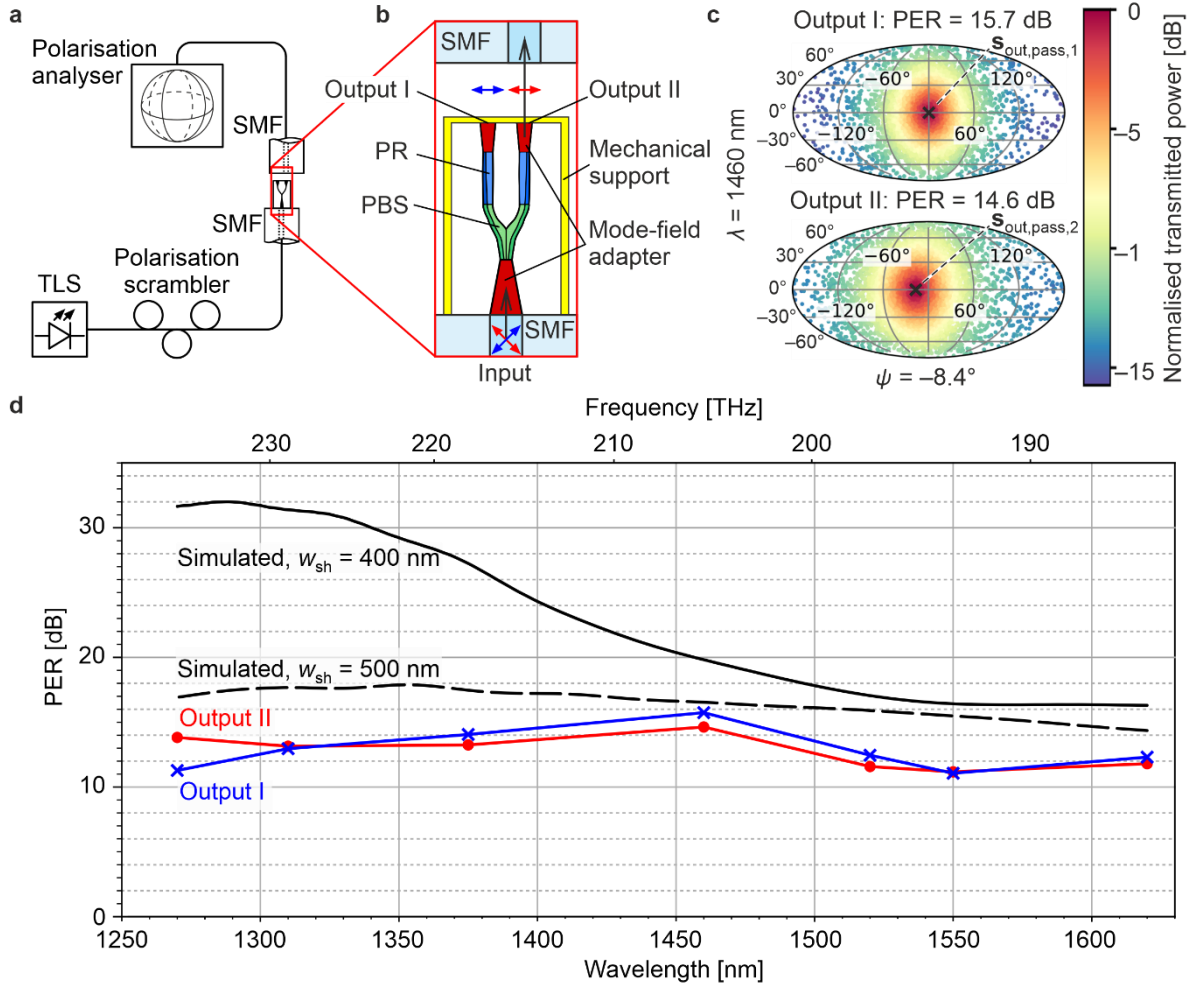
Figure S2: Measurement of the polarisation extinction ratio (PER) of the PBS with attached polarisation rotators (PR).
a, Experimental setup: The PBS is 3D-printed together with the PR and additional mode-field adapters on the facet of an SMF, which is connected to a polarisation scrambler. The two output ports are probed by a movable SMF, which is attached to a polarisation analyser. The polarisation at the input is scrambled randomly, and the power and the Stokes vector of the output polarisation state is measured at both outputs. **B,** Schematic rendering of the PBS (green) with attached PR (blue) and mode-field adapters (red), which are attached to a table-like mechanical support structure (yellow). Orthogonal polarisation states (blue and red arrows) at the input port are separated to identical polarisation states at the output of the structure. **C,** Measured output Stokes states on the Poincaré sphere in Mollweide projection, coloured by normalised transmitted power. For simplicity, we rotate all measured Stokes vectors such that the polarisation state with highest transmitted power at Output I, $s_{out,pass,1}$, is oriented along the s_1-direction of the Poincaré sphere (0° longitude and 0° latitude), which corresponds to a linear polarisation in horizontal direction, while the predominant polarisation state at Output II, $s_{out,pass,2}$, is on the equator of the Poincaré sphere, corresponding to a linear polarisation at a certain angle ψ with respect to the horizontal direction. We extract only a slight angle deviation of $\psi = -8.4°$ of the two equivalent linear polarisation states, indicating correct operation of the PR. **d,** Measured and simulated PER. The measured PER for both outputs (blue and red solid lines) exceed 11dB over the full wavelength range of 350 nm. The black lines show PER simulation results for the structure without mode-field adapters at the outputs. Specifically, the solid black line represents simulation results for the designed structure with a nominal smaller dimension $w_{sh} = 400$ nm of the fabricated partial waveguides WG$_H$ and WG$_V$, see Fig. 2a of the main manuscript. In contrast to this, the dashed black line represents the behaviour of a structure, for which w_{sh} is increased to 500 nm due to fabrication tolerances. We find that this increase can well explain the measured behaviour.

of the PBS/PR. This needs to be considered when evaluating the measurement data, see Section S4 for details. Note also that the two output ports of our structure are only separated by 25 μm, and we may hence assume that the polarisation rotation in the SMF does not change significantly when moving the SMF between the ports. For an ideal device, the two ports should thus exhibit maximum transmission at identical output polarisation states.

The measurement results obtained from our test structure at a wavelength of $\lambda = 1460$ nm are depicted in Fig. S2c. For this measurement, the input polarisation state was scanned across 20 000 points uniformly distributed on the Poincaré sphere. The plot shows the measured Stokes states on the Poincaré sphere in Mollweide projection, coloured by normalised transmitted power. For each of the two device outputs, we find a predominant polarisation state, which we mark by $\mathbf{s}_{\mathrm{out,pass,1}}$ and $\mathbf{s}_{\mathrm{out,pass,2}}$ in Fig. S2c. These states correspond to the polarisation that would be transmitted to the respective output of a perfect PBS/PR. For a real device with finite PER, the output polarisation states $\mathbf{s}_{\mathrm{out,pass,1}}$ and $\mathbf{s}_{\mathrm{out,pass,2}}$ exhibit the highest power transmission. At the same time, the measured output polarisation states are concentrated around $\mathbf{s}_{\mathrm{out,pass,1}}$ and $\mathbf{s}_{\mathrm{out,pass,2}}$ in case the input polarisation is randomly varied. Note that, for simplicity, we rotated all measured Stokes vectors such that $\mathbf{s}_{\mathrm{out,pass,1}}$ is oriented along the s_1 -direction (latitude 0° and longitude 0°), which corresponds to a linear polarisation in horizontal direction, while $\mathbf{s}_{\mathrm{out,pass,2}}$ is on the equator of the Poincaré sphere, corresponding to a linear polarisation at a certain angle ψ with respect to the horizontal direction. Note also that the transformation of the measured output polarisations to linear polarisation states is somewhat arbitrary since the true polarisation transformation in the output fibre is unknown. Still, we extract only a slight angle deviation of $\psi = -8.4°$ of the two equivalent linear polarisation states, indicating a fairly good performance of the PR.

For each of the output ports, we then extract the polarisation extinction ratio (PER), which is here defined as the ratio of the maximum transmitted power at the target output polarisation state to the minimum power at the antipodal point on the Poincaré sphere. For better reliability of the extracted results, we implemented a PER evaluation technique that considers all power levels recorded for the various input polarisation states rather than just the maximum and the minimum power, see Section S4 for details. The experiment was repeated for different wavelengths over a broad range from 1270 nm to 1620 nm, see Fig. S2d (the same experimental data is shown in Fig. 4b of the main manuscript) for a plot of the extracted PER vs. wavelength. We find that the PER is better than 11 dB over the whole wavelength range, which was only limited by the tuning range of the underlying external-cavity lasers, (Ando AQ4321D, TUNICS T1005-HP, and Agilent 81600B). We also measured the insertion loss of the device using the polarisation state of maximum transmission at each output port. At a wavelength of 1550 nm, we find losses of 4.4 dB and 3.8 dB for Output I and Output II, respectively.

Both the measured PER and insertion loss are slightly worse than the performance expected by simulations, see Fig. 2c of the main manuscript. Note, however, that the measured values include the loss of the PBS, of the subsequent PR, and of the adiabatic mode-field adapters at the input and the output of the device, whereas Fig. 2c of the main manuscript refers to a simulation of the PBS section only. To benchmark our measurements, we simulated S-parameters and the PER for the full structure consisting of the PBS/PR and the mode-field adapter at the input port. To account for typical fabrication tolerances and to understand the impact of limited lithography resolution on the device performance, we considered two values w_{sh} = 400 nm and w_{sh} = 500 nm of the smaller dimension w_{sh} of the partial waveguides WG$_{\mathrm{H}}$ and WG$_{\mathrm{V}}$ as defined in Fig. 2a of the main manuscript, see also Section S1. The results for the PER are depicted as solid and dashed black line in Fig. S2. As expected from our considerations described in Section S1, we find that the increase of w_{sh} from 400 nm to 500 nm reduces the PER, while the transmission remains essentially unchanged. Specifically, the simulated PER for w_{sh} = 500 nm coincides quite well with the measured values, supporting the notion that limited lithographic resolution is the most likely cause for the performance deviation between the

fabricated and the designed structure. The transmission simulated for the full structure at a wavelength of 1550 nm amounts to −1.42 dB for w_{sh} = 400 nm and to −1.59 dB for w_{sh} = 500 nm and is hence much lower than the measured values of −4.4 dB (Output I) and −3.8 dB (Output II). Note that the transmission of −1.42 dB and −1.59 dB simulated for the full structure for w_{sh} = 400 nm and w_{sh} = 500 nm, respectively, is even slightly higher than the values of −1.55 dB and −1.75 dB obtained for the corresponding PBS only, see Section S1. We hence conclude that the mode-field adapter at the input and the PR at the outputs do not introduce any noticeable penalty, and we attribute the slightly lower loss obtained from the simulation of the full structure to modelling inaccuracies and to propagation of spurious higher-order modes in the PR section.

While these results demonstrate the viability and the performance of the proposed approach, there is clearly room for improvement. Regarding the PER, we expect that exploiting super-resolution 3D-lithography inspired by the concept of stimulated-emission-depletion (STED)[4] microscopy might allow to better resolve fine details of the PBS structure and to enhance the performance. For the insertion loss, we still find a substantial deviation between the measured insertion losses of 4.4 dB and 3.8 dB for Output I and Output II, respectively, and their sub- 2 dB counterparts obtained from the simulation of the full structure. We believe that the substantial part of the approx. 2.5 dB loss overhead originates from the surface roughness on the approximately 80 µm long 45° PR. Based on our previously achieved insertion loss figures of overclad 3D-printed photonic wire-bonds[1], we believe that a selective cladding of the connecting waveguides and the mode-field adapters could reduce the insertion loss overhead to approx. 1 dB and therefore bring down the insertion loss of the whole assembly to about 2.5 dB.

S3. Scattering parameters, Jones matrix, and polarisation extinction ratio (PER)

Figure 2c of the main manuscript gives the simulated PBS performance in terms of transmission, crosstalk, leakage, unfilterable crosstalk, and PER. The first four parameters are directly extracted from the corresponding elements of the simulated scattering matrix, as indicated in Fig. 2c and in the main text. For calculating the PER, we use the ratio of the squares of the singular values of the simulated Jones matrices of the PBS[5]. The Jones matrix associated with a certain output port describes the propagation of light from the PBS input port to this output port. In the following, the Jones matrix associated with output port H is denoted as $\mathbf{T}_{\text{PBS},H}$, while $\mathbf{T}_{\text{PBS},V}$ refers to output port V. The Jones vector at the input port is $\mathbf{J}_I = \begin{bmatrix} E_H^{(I)} & E_V^{(I)} \end{bmatrix}^{\text{T}}$, while the Jones vectors at the output ports H and V are $\mathbf{J}_H = \begin{bmatrix} E_H^{(H)} & E_V^{(H)} \end{bmatrix}^{\text{T}}$ and $\mathbf{J}_V = \begin{bmatrix} E_H^{(V)} & E_V^{(V)} \end{bmatrix}^{\text{T}}$. The Jones-matrix elements can be directly taken from the scattering matrix, such that the relations $\mathbf{J}_H = \mathbf{T}_{\text{PBS},H}\,\mathbf{J}_I$ and $\mathbf{J}_V = \mathbf{T}_{\text{PBS},V}\,\mathbf{J}_I$ between the Jones vectors at the input and at the output can be written as

$$\begin{bmatrix} E_H^{(H)} \\ E_V^{(H)} \end{bmatrix} = \begin{bmatrix} \underline{S}_{E_H^{(H)}E_H^{(I)}} & \underline{S}_{E_H^{(H)}E_V^{(I)}} \\ \underline{S}_{E_V^{(H)}E_H^{(I)}} & \underline{S}_{E_V^{(H)}E_V^{(I)}} \end{bmatrix} \begin{bmatrix} E_H^{(I)} \\ E_V^{(I)} \end{bmatrix}, \tag{S1}$$

$$\begin{bmatrix} E_H^{(V)} \\ E_V^{(V)} \end{bmatrix} = \begin{bmatrix} \underline{S}_{E_H^{(V)}E_H^{(I)}} & \underline{S}_{E_H^{(V)}E_V^{(I)}} \\ \underline{S}_{E_V^{(V)}E_H^{(I)}} & \underline{S}_{E_V^{(V)}E_V^{(I)}} \end{bmatrix} \begin{bmatrix} E_H^{(I)} \\ E_V^{(I)} \end{bmatrix}. \tag{S2}$$

The PER is then calculated as the ratio of the squares of the singular values s_1 and s_2 of the corresponding Jones matrices,[5]

$$\text{PER} = \frac{s_1^2(\mathbf{T}_{\text{PBS},H})}{s_2^2(\mathbf{T}_{\text{PBS},H})} = \frac{s_1^2(\mathbf{T}_{\text{PBS},V})}{s_2^2(\mathbf{T}_{\text{PBS},V})}, \tag{S3}$$

where $s_1 \geq s_2$ without loss of generality.

## S4. PER extraction from the measurements

The PER of an optical device is generally defined as the ratio of maximum to minimum output power P_{out} that can be found when varying the input polarisation over all possible states. In our experiments, the input polarisation states were sampled randomly, and a straightforward way of calculating the PER is taking the ratio of the maximum to the minimum recorded output power. However, this approach takes into account only two measured power levels, which bears the risk that the result is subject to noise, which could lead to an overestimated PER. In addition, there is no guarantee that the sampled input states will fall close enough to the states of minimum and maximum transmitted power.

We therefore implemented a PER evaluation technique that considers all power levels recorded for the various input polarisation states and relies on fitting a theoretical curve to the full set of measurement data. To explain this technique, we consider only one output port of the 3D-printed polarisation-beam-splitter/polarisation-rotator combination (PBS/PR) – the other output port can be treated in an analogous way. We represent four-dimensional normalised Stokes vectors $\mathbf{S} = [1 \quad S_1/S_0 \quad S_2/S_0 \quad S_3/S_0]^{\mathrm{T}}$ by the corresponding three-dimensional Stokes vectors $\mathbf{s} = [s_1 \quad s_2 \quad s_3]^{\mathrm{T}}$, where $s_1 = S_1/S_0$, $s_2 = S_2/S_0$, and $s_3 = S_3/S_0$, that can be represented in the Cartesian coordinate system of the Poincaré sphere, see Section 14.5 of Ref. [6]. For simplicity, we further assume that the maximum power transmission for the considered port occurs for a perfectly horizontal (*x*-polarised) polarisation at both the input and the output of the PBS/PR, characterised by three-dimensional Stokes vectors $\mathbf{s}_{\mathrm{in,pass}} = \mathbf{s}_{\mathrm{out,pass}} = [1 \quad 0 \quad 0]^{\mathrm{T}}$. Note that the input port can only be accessed through an optical fibre that is connected to the polarisation scrambler, and that the measurement of the power and the polarisation state at the PBS/PR output requires a second optical fibre leading to the polarisation analyser, see Fig. S3a for a sketch of the experimental setup. In the following, we assume fully polarised light such that we can use either Stokes or Jones calculus, as appropriate. We describe the input fibre between the polarisation scrambler and the PBS/PR by a Jones matrix $\mathbf{U}$, whereas the output fibre is described by a Jones matrix $\mathbf{V}$, see Fig. S3a. For a given polarisation state with Jones vector $\mathbf{J}_{\mathrm{scr}}$ emitted by the polarisation scrambler, the Jones vector of the polarisation state $\mathbf{J}_{\mathrm{an}}$ received by the polarisation analyser can then be written as

$$\mathbf{J}_{\mathrm{an}} = \mathbf{V}\,\mathbf{T}_{\mathrm{PBS}}\,\mathbf{U}\,\mathbf{J}_{\mathrm{scr}}, \tag{S4}$$

where $\mathbf{T}_{\mathrm{PBS}}$ corresponds to the Jones matrix of the non-ideal PBS/PR, and where the Jones matrices $\mathbf{U}$ and $\mathbf{V}$ of the input fibre and the output fibre can be assumed to be unitary, see Fig. S3a. The light at the PBS/PR input can be expressed by an input Jones vector $\mathbf{J}_{\mathrm{in}} = \mathbf{U}\,\mathbf{J}_{\mathrm{scr}}$, which is characterised by an angle α_{in} that defines the ratio of the field amplitudes in the two polarisations and by a phase difference φ between the *x*- and the *y*-component,

$$\mathbf{J}_{\mathrm{in}} = \underline{E}_{\mathrm{in}} \begin{bmatrix} \cos(\alpha_{\mathrm{in}})e^{-\mathrm{j}\varphi/2} \\ \sin(\alpha_{\mathrm{in}})e^{+\mathrm{j}\varphi/2} \end{bmatrix}. \tag{S5}$$
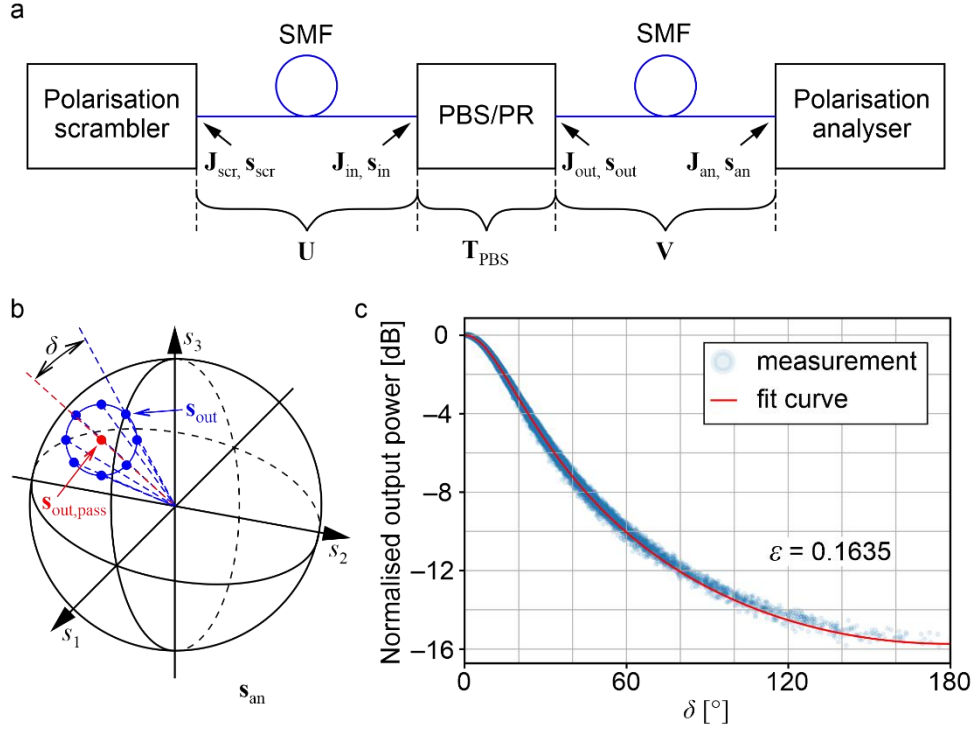
Figure S3: Measurement and evaluation of the polarisation extinction ratio (PER) of the 3D-printed polarisation-beam-splitter/polarisation-rotator (PBS/PR) combination, taking into account the full set of measured output powers and polarisation states. a, Experimental setup: Light emitted from a polarisation scrambler is fed to the 3D-printed PBS/PR through a standard single-mode fibre (SMF), and the output power and the output polarisation state are measured by a polarisation analyser, which is connected to the PBS/PR by a second SMF. $\mathbf{J}_{scr}, \mathbf{J}_{in}, \mathbf{J}_{out}$, and $\mathbf{J}_{an}$ denote the Jones vectors at the output of the polarisation scrambler, the input and the output of the PBS/PR, and at the input of the polarisation analyser, respectively, and $\mathbf{s}_{scr}$, $\mathbf{s}_{in}, \mathbf{s}_{out}$, and $\mathbf{s}_{an}$ are the corresponding Stokes vectors. Note that we represent four-dimensional normalised Stokes vectors $[1 \quad S_1/S_0 \quad S_2/S_0 \quad S_3/S_0]^T$ by the corresponding three-dimensional Stokes vectors $\mathbf{s} = [s_1 \quad s_2 \quad s_3]^T$, where $s_1 = S_1/S_0, s_2 = S_2/S_0$, and $s_3 = S_3/S_0$, that can be represented in the Cartesian coordinate system of the Poincaré sphere. The non-ideal PBS/PR is modelled by a Jones matrix $\mathbf{T}_{PBS}$, while the two SMF at the input and the output side of the PBS/PR are represented by two unitary Jones matrices $\mathbf{U}$ and $\mathbf{V}$, respectively. **b,** Illustration of the three-dimensional vectors $\mathbf{s}_{out}$ recorded by the polarisation analyser. Since we assume fully polarised light, all vectors are on the surface of the Poincaré sphere. The output power should be the same for all polarisation states that are located on a circle, which is centred about the state of maximum transmission. The radius of this circle is quantified by the opening angle δ of the associated cone, which can be directly connected to the normalised output power. **c,** Normalised output power P_{out}/P_{in} vs. angle δ, as recorded for the data point for Output 1 at a wavelength of 1460 nm, see Fig. S2d. By fitting a model function (red) to the measurement data (blue), we extract a polarisation leakage magnitude of $\varepsilon = 0.1635$, corresponding to a PER of 15.7 dB.

In this relation, $\underline{E}_{in}$ denotes the electric field that is associated with the signal at the input of the 3D-printed PBS/PR – the corresponding power is denoted by $P_{in} \sim |\underline{E}_{in}|^2$. For the PBS/PR, we assume a simplified Jones matrix $\mathbf{T}_{PBS}$ that corresponds to that of a non-ideal linear polariser oriented along the *x*-direction,

$$\mathbf{T}_{PBS} = \begin{bmatrix} 1 & 0 \\ 0 & \varepsilon \end{bmatrix}, \tag{S6}$$

where $\varepsilon, 0 \leq \varepsilon \leq 1$, is the magnitude of the polarisation leakage. The corresponding PER is then found as the ratio of the squares of the singular values of $\mathbf{T}_{PBS}$[5]

$$\mathrm{PER} = \frac{1}{\varepsilon^2}. \tag{S7}$$

Note that the model for the Jones matrix according to Eq. (S6) represents an approximation: The Jones matrices $\mathbf{T}_{PBS,H}$ and $\mathbf{T}_{PBS,V}$ that are obtained from our simulations, Eqs. (S1) and (S2), do have non-zero off-diagonal elements and are generally not Hermitian. As a consequence, transformation into a

diagonal matrix as assumed in Eq. (S6) is not generally possible. Still, the magnitudes of the off-diagonal elements are small such that the associated error should not be severe, see discussion below.

Using the Jones-matrix model according to Eq. (S6), the relation between a given polarisation state, $\mathbf{J}_{\text{in}}$ at the input of the PBS/PR and the corresponding output state $\mathbf{J}_{\text{out}}$ can be written as

$$\mathbf{J}_{\text{out}} = \mathbf{T}_{\text{PBS}} \cdot \mathbf{J}_{\text{in}} = \underline{E}_{\text{in}} \begin{bmatrix} \cos(\alpha_{\text{in}})e^{-\text{j}\varphi/2} \\ \varepsilon \sin(\alpha_{\text{in}})e^{+\text{j}\varphi/2} \end{bmatrix}. \tag{S8}$$

We can now express the ratio of the power P_{out} at the output of the PBS/PR to the input power P_{in} in terms of the magnitude of the polarisation leakage ε and the angle α_{in},

$$\frac{P_{\text{out}}}{P_{\text{in}}} = \frac{|\mathbf{J}_{\text{out}}|^2}{|\mathbf{J}_{\text{in}}|^2} = \cos^2(\alpha_{\text{in}}) + \varepsilon^2 \sin^2(\alpha_{\text{in}}). \tag{S9}$$

Note that the ratio in Eq. (S9) does not depend on the phase difference φ.

When evaluating the measurement, we face the problem that the angle α_{in} and thus the expression for the power transmission according to Eq. (S9) are related to the Jones vector at the output of the PBS/PR, which cannot be accessed in the measurement. To establish a relationship to the known polarisation state $\mathbf{J}_{\text{an}}$ at the input of the polarisation analyser, we proceed in two steps. First, we switch to Stokes space, and we find a relationship that connects the angle α_{in} and the magnitude of the polarisation leakage ε in Eq. (S8) to the angle δ between the actual three-dimensional Stokes vector $\mathbf{s}_{\text{out}}$ at the PBS/PR output and the three-dimensional Stokes vector $\mathbf{s}_{\text{out,pass}} = \begin{bmatrix} 1 & 0 & 0 \end{bmatrix}^{\text{T}}$ that corresponds to maximum transmission. To this end, we first calculate $\mathbf{s}_{\text{out}} = \begin{bmatrix} s_{\text{out,1}} & s_{\text{out,2}} & s_{\text{out,3}} \end{bmatrix}^{\text{T}}$ from the components of vector $\mathbf{J}_{\text{out}}$ using Eqs. (6.1-9a)–(6.1-9d) in Ref. [7]. The angle $\delta \in [0, \pi]$ between the measured three-dimensional Stokes vector $\mathbf{s}_{\text{out}}$ and the three-dimensional Stokes vector $\mathbf{s}_{\text{out,pass}} = \begin{bmatrix} 1 & 0 & 0 \end{bmatrix}^{\text{T}}$ of maximum transmission can then be calculated as

$$\cos(\delta) = \mathbf{s}_{\text{out}} \cdot \mathbf{s}_{\text{out,pass}} = s_{\text{out,1}} = \frac{\cos^2(\alpha_{\text{in}}) - \varepsilon^2 \sin^2(\alpha_{\text{in}})}{\cos^2(\alpha_{\text{in}}) + \varepsilon^2 \sin^2(\alpha_{\text{in}})}, \tag{S10}$$

which can be simplified to

$$\tan\left(\frac{\delta}{2}\right) = \varepsilon \tan(\alpha_{\text{in}}). \tag{S11}$$

In a second step, we then account for the propagation of the signal from the PBS/PR output to the polarisation analyser. To this end, we exploit the fact that the corresponding Jones vectors $\mathbf{J}_{\text{out}}$ and $\mathbf{J}_{\text{an}}$ are related by a unitary transformation that is described by the Jones matrix $\mathbf{V}$ of the output fibre. In the Cartesian coordinate system of the Poincaré sphere, this transformation simply corresponds to a rotation about the origin, which leaves the relative angle δ between the measured vectors $\mathbf{s}_{\text{out}}$ and $\mathbf{s}_{\text{out,pass}}$ unchanged. In other words: For a given polarisation leakage magnitude ε, the output power P_{out} should be the same for all polarisation states that are located on a circle on the surface of the Poincaré sphere which is centred about $\mathbf{s}_{\text{out,pass}}$, see Fig. S3b for an illustration. We may thus extract this angle directly from the polarisation states recorded at the polarisation analyser, where $\mathbf{s}_{\text{out,pass}}$ corresponds to polarisation state for which the highest output power was measured. We then use Eq. (S11) with ε as a parameter to extract α_{in} and predict the dependence of the power P_{out} on δ via Eq. (S9), assuming constant P_{in}. We finally vary the magnitude of the polarisation leakage ε to find best coincidence between the measured δ-dependence of P_{out} and the associated model prediction, see Fig. S3c. Equation (S7) then allows us to calculate the PER for this value of ε.
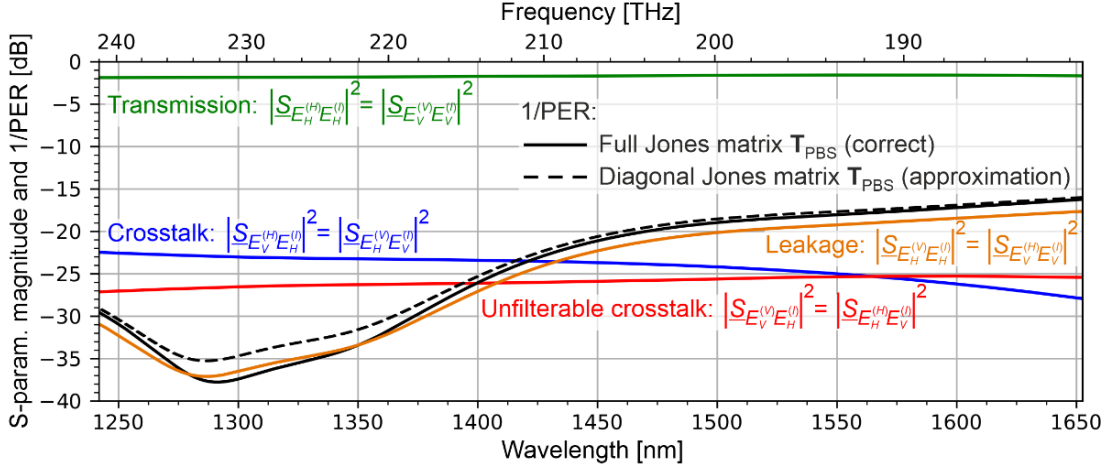
Figure S4: Comparison of PER extracted from the simulated Jones matrices without any off-diagonal elements according to the simplified model in Eq. (S6) (dashed black lines) and the PER extracted from the full Jones matrix (solid black line). The device is the same as the one described by Fig. 2c of the main manuscript. For better comparison, we also give the transmission, the crosstalk, the leakage, and the unfilterable crosstalk of the device – they are identical to the curves in Fig. 2c of the main manuscript.

We show the results of this technique in Fig. S2c for the highest PER that we measured during our wavelength sweep, i.e., for Output 1 at a wavelength of 1460 nm, see Fig. S2d. From the least-squares model fit shown in Fig. S3c, we estimate a field leakage ε of 0.1635, corresponding to a PER of 15.7 dB. To check the validity of the approach, we also extract the PER by simply taking the ratio of the maximum and the minimum transmitted power, which leads to value of 16.1 dB. This confirms the validity of our approach, in particular with respect to the simplified model for the Jones matrix according to Eq. (S6). The result is also in line with the expectation that the PER extracted from the ratio of the maximum and the minimum transmitted power might be slightly overestimated due to measurement noise. We further checked the impact of neglecting the off-diagonal Jones-matrix elements in Eq. (S6) by simulations. To this end, we omit the elements $\underline{S}_{E_H^{(H)}E_V^{(I)}}$, $\underline{S}_{E_V^{(H)}E_H^{(I)}}$, $\underline{S}_{E_H^{(V)}E_V^{(I)}}$, and $\underline{S}_{E_V^{(V)}E_H^{(I)}}$ of the simulated Jones matrices according to Eqs. (S1) and (S2) and then extract the PER via Eq. (S7). The resulting PER is then compared to the one extracted from the singular values of the full Jones matrices, see Fig. S4. We find that omitting the off-diagonal Jones-matrix elements leads to a slight reduction of the extracted PER, and we conclude that the simplification related to Eq. (S6) does not bear the risk to overestimate the PER in our experiments.

S5. Data transmission experiment

The setup used for data transmission experiment is depicted in Fig. S5. To generate a 16QAM data stream at a symbol rate of 80 GBd, a dual-polarisation (DP) IQ modulator is driven by a high-speed arbitrary waveform generator (AWG, Keysight M8194A 120 GSa/s) using random bit sequences with different seeds for each polarisation. The optical carrier at a wavelength of 1550 nm is provided by an external-cavity laser (ECL, Keysight N7714A, emission frequency f_c in Inset 1 of Fig. S5). Root-raised-cosine pulse shaping at a roll-off factor of $\beta = 0.1$ is used for good spectral efficiency. At a BER of 1.25×10^{-2}, which corresponds to the threshold of forward error correction with 15 % coding overhead, see Table 7.5 in Ref. [8], our transmission setup exhibits an OSNR penalty of approximately 3 dB with respect to an ideal transmission system, see Fig. 4d of the main manuscript. This is in accordance with values in literature for similar modulation formats and symbol rates[9].
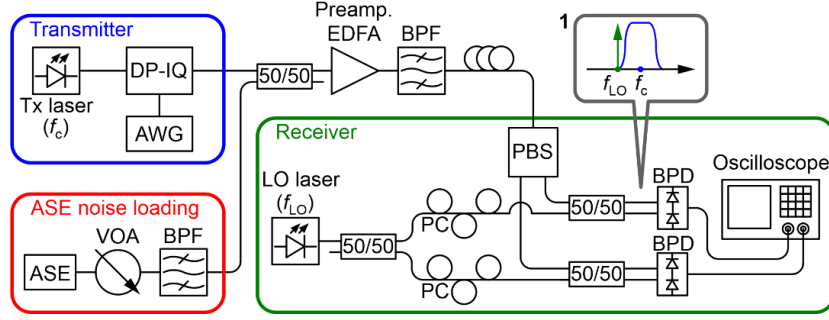
Figure S5: Experimental setup for the data-transmission demonstration: An optical carrier at $\lambda = 1550$ nm (frequency f_c) is modulated by a dual polarisation IQ (DP-IQ) modulator that is driven by an arbitrary waveform generator (AWG) to generate a 16QAM PDM signal at 80 GBd. The band-limited amplified-spontaneous-emission (ASE) source generates noise, whose power is varied by a variable optical attenuator (VOA), and added to the 16QAM signal. This noise-loaded data signal is amplified by an EDFA, filtered by a bandpass filter (BPF), and guided to the PBS input in the receiver block. A local oscillator (LO) signal (frequency f_{LO}) is split, and the two split signals are sent through a pair of polarisation controllers (PC) and superimposed with the two output signals of the PBS in a pair of balanced photodetectors (BPD). The electrical output signals are detected by a high-speed oscilloscope. Inset 1 illustrates the spectrum at the BPD inputs, with the LO tone tuned to the edge of the signal for heterodyne detection.

For the OSNR sweep at the receiver, band-limited amplified stimulated emission (ASE) noise is generated by a dedicated ASE noise source (Orion Laser Technology ASE-C/CL) and added to the optical signal (ASE noise loading). The noise-loaded signal is then amplified by an EDFA, filtered by a bandpass filter (BPF, full width at half maximum 1 nm) to suppress out-of-band amplified ASE noise, and sent to the PBS, which may be either a 3D-printed PBS/PR assembly or a commercial fibre-based PBS that we use as a reference. After the PBS, each polarisation is detected using a coherent heterodyne scheme, where the local oscillator laser (LO, Keysight N7714A, emission frequency f_{LO}) is tuned to the low-frequency edge of the signal spectrum, see in Inset 1 of Fig. S5. Two balanced photodetectors (BPD, Finisar BPDV2150RQ) are used to suppress both signal-signal and LO-LO mixing products. The outputs of the BPD are digitised by a 256 GSa/s real-time oscilloscope (Keysight UXR1004A) and recorded for offline digital signal processing (DSP). In a first DSP step, the signals are made analytic and are shifted in frequency by the difference between the carrier and the LO. After timing recovery, a 2 × 2 MIMO equaliser is used for polarisation de-multiplexing, and afterward the carrier recovery is performed. The MIMO equaliser is an adaptive equaliser, whose coefficients are updated according to the radius directed equalisation (RDE)[10]. Finally, the signals go through a least-mean-square equaliser before being decoded. To benchmark the performance of the PBS/PR assembly, the experiment is also performed with a commercially available PBS (AFW Technologies, POBS-15). Since the commercially available PBS exhibits less insertion loss than the PBS/PR-fanout assembly, we adjust the amplification of the preamplifier to obtain equal powers at the inputs of the BPD in both cases. They key finding of our experiment is that the 3D-printed PBS/PR assembly does not introduce any additional OSNR penalty with respect to the commercial PBS, see Fig. 4d and the discussion thereof in the main manuscript.

Note that the somewhat unusual heterodyne reception scheme was chosen instead of a more common intradyne scheme because we only had two balanced photodetectors with sufficient bandwidth available at the time of the experiment. However, we paid a price in terms of the OSNR implementation penalty of our 16AM transmission system, which amounts to approximately 3 dB at a bit-error ratio (BER) of 1.25×10^{-2}, see Fig. 4d of the main manuscript. This is caused by the fact that the BPF in front of the receiver has only a roll-off with finite steepness such that it cannot fully suppress the ASE components at frequencies below the LO tone. These unsuppressed noise components are also down-

converted to the signal band and essentially add to the noise components resulting from ASE noise at the high-frequency side of the LO tone, thus leading to a reduction of the SNR by approximately 2 dB with respect to that expected for an ideal intradyne receiver. Using a standard intradyne receiver with four balanced detectors would therefore allow to reduce the OSNR penalty from the currently observed 3 dB to approximately 1dB, which is a typical value found for other laboratory-type 16QAM transmission systems in the literature[11]. Still, since the transmission experiments with the commercial PBS and the 3D-printed PBS were done with the same system and were hence both subject to the same additional ASE noise. The results shown in Fig. 4 hence still confirm the excellent performance of our 3D-printed PBS.

It should also be noted that the assembly shown in Fig. 4a of the main manuscript was designed for simple fabrication and characterisation, allowing to measure the PER at the interface between the PBS/PR structure and the fan-out. It hence differs from the arrangement illustrated in Fig. 1, where the PBS/PR is integrated into a photonic-wire-bond interface between an SMF and a silicon photonic circuit, and where polarisation analysis at the PBS/PR outputs would be impossible. Moreover, implementing the assembly shown in Fig. 1 would require further process optimisation, e.g., with respect to lithographic resolution, which exhibits a slight anisotropy such that the orientation of the writing beam with respect to the structure plays an important role. Approaches on how to improve the lithography resolution are discussed in Section S2.

S6. PBS performance for variations of geometry parameters

To quantify the sensitivity of the PBS performance with respect to deviations from the design shown in Fig. 2 of the main manuscript, we vary several geometry parameters of the structures and re-calculate the key performance metrics discussed the main manuscript, i.e., the transmission $\left|\underline{S}_{E_H^{(H)}E_H^{(I)}}\right|^2 = \left|\underline{S}_{E_V^{(V)}E_V^{(I)}}\right|^2$, the crosstalk $\left|\underline{S}_{E_V^{(H)}E_H^{(I)}}\right|^2 = \left|\underline{S}_{E_H^{(V)}E_V^{(I)}}\right|^2$, the unfilterable crosstalk $\left|\underline{S}_{E_H^{(H)}E_V^{(I)}}\right|^2 = \left|\underline{S}_{E_V^{(V)}E_H^{(I)}}\right|^2$, the leakage $\left|\underline{S}_{E_H^{(V)}E_H^{(I)}}\right|^2 = \left|\underline{S}_{E_V^{(H)}E_V^{(I)}}\right|^2$, and the polarisation extinction ratio (PER). The geometry parameters that were subjection to variations are depicted in red in Fig. S6a, and the resulting changes of the PBS performance parameters obtained for light with a vacuum wavelength of 1550 nm are depicted in Fig. S6b, c, d, and e. In each variation of one geometry parameter, the others are kept at their respective initial values that were used for the PBS structure analysed in Fig. 2 of the main manuscript and that are indicated by dashed vertical lines in Fig. S6b, c, d, and e. Note that the length L_A of Section A of the device does not play an important role for the device performance, and we did hence not vary it in this simulation series. With respect to L_A, the only important condition is that the mode-field at the circular input is adiabatically morphed into the corresponding mode-field at the cross-like cross-section. In our device L_A was only 5 µm long, which was sufficient for adiabatic morphing of the input mode field.

In a first step, we vary the short side w_{sh} and the long side $w_{lo,max}$ of the cross section of the partial waveguides WG_H and WG_V, see Fig. S6b and c. We find that the PER decreases with smaller aspect ratio $w_{lo,max}/w_{sh}$, i.e., with smaller $w_{lo,max}$ and with bigger w_{sh}, which is consistent with PER degradation observed in Fig. S1 as a consequence of a reduced aspect ratio. The remaining performance metrics remain largely unaffected, with a small decrease of the transmission with bigger w_{sh} and bigger $w_{lo,max}$, which we attribute to the increasing multi-mode behaviour of the partial waveguides and hence higher
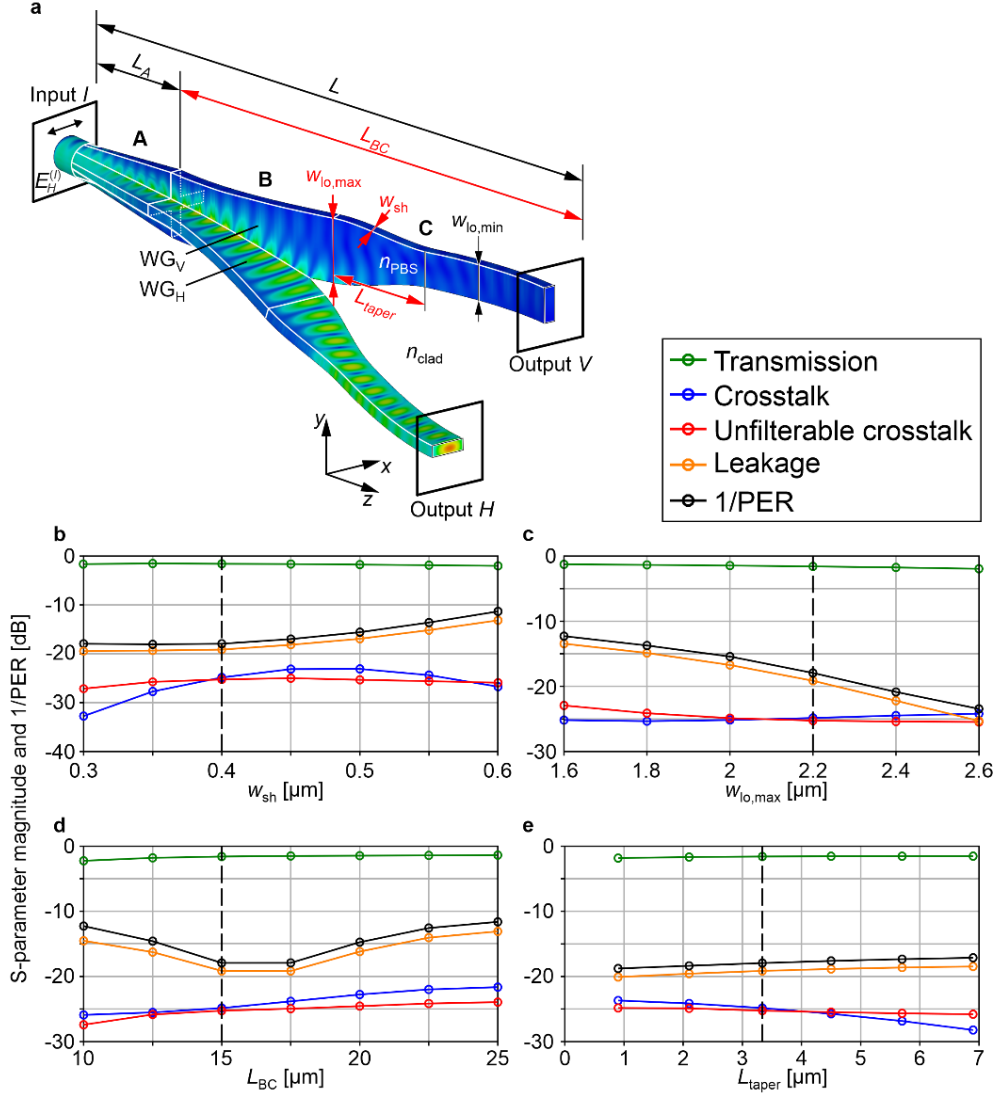
Figure S6: Simulated performance of the PBS under variations of geometry parameters at a wavelength of 1550 nm. In each variation of one geometry parameter in Subfigures b–e, the other parameters are kept at their respective initial values that were used for the PBS structure analysed in Fig. 2 of the main manuscript and that are indicated by dashed vertical lines in the respective subfigure. **a,** 3D model of the PBS with studied geometry parameters marked in red. The performance metrics includes the transmission $\left|\underline{S}_{E_H^{(H)}E_H^{(I)}}\right|^2 = \left|\underline{S}_{E_V^{(V)}E_V^{(I)}}\right|^2$, the crosstalk $\left|\underline{S}_{E_V^{(H)}E_H^{(I)}}\right|^2 = \left|\underline{S}_{E_V^{(V)}E_V^{(I)}}\right|^2$, the unfilterable crosstalk $\left|\underline{S}_{E_H^{(H)}E_V^{(I)}}\right|^2 = \left|\underline{S}_{E_V^{(V)}E_H^{(I)}}\right|^2$, the leakage $\left|\underline{S}_{E_H^{(V)}E_H^{(I)}}\right|^2 = \left|\underline{S}_{E_V^{(H)}E_V^{(I)}}\right|^2$, and the polarisation extinction ratio (PER), see also Fig. 2 in and the discussion thereof in the main manuscript. **b,** Sensitivity of performance metrics on the short side w_{sh} of the rectangular high-aspect-ratio waveguide cross-section. **c,** Sensitivity on the short on the long side $w_{lo,max}$. The PER decreases with smaller aspect ratio $w_{lo,max}/w_{sh}$, i.e., with smaller $w_{lo,max}$ and bigger w_{sh}. **d,** Sensitivity on the combined length L_{BC} of the Sections B and C. The border between Sections B and C is defined and fixed as a 44th percentile of L_{BC}. **e,** Sensitivity on length L_{taper}, of the taper in Section C. The taper begins at the border between Sections B and C, and the taper end is defined as a percentile of L_{BC} bigger than 44% and smaller than 100%, for a fixed L_{BC}. Variations of L_{BC} and L_{taper} of the order several micrometres do not significant influence on device performance, thereby confirming the robustness of the concept and the associated design.

losses of power to higher-order modes. In Fig. S6d, we investigate the impact of a variation of the length L_{BC}, which is the combined length of Sections B and C of the device, $L_{BC} = L_B + L_C$. We find that for the overall length L_{BC} the currently used value of 15 μm seems to be a good choice, and that larger changes of the order of a few micrometres can be tolerated while leaving the structure performance largely intact, see Fig. S6d. Finally, we varied the length L_{taper} of the taper in Section C of the device. The beginning of the taper corresponds with the transition between Sections B and C, which is fixed at 44% of the length L_{BC}, measured from the beginning of Section B. The end of the taper is defined as a

percentile between 44% (beginning of Section C) and 100% (end of Section C). In our study, we varied this percentile from 50% to 90%, which corresponded to taper lengths from 0.9 µm to 6.9 µm. It can be seen on Fig. S6e that the device performance is rather insensitive to variations of L_{taper} of the order of several micrometres. Overall, our simulations shown that, except for the aspect ratio of the rectangular partial waveguides, the PBS design proposed and described in the main manuscript is fairly robust with respect to geometry variations and should hence be amenable to high-throughput mass production by in-situ laser printing.

References

1. Blaicher, M. *et al.* Hybrid multi-chip assembly of optical communication engines by in situ 3D nano-lithography. *Light Sci. Appl.* **9**, 71 (2020).

2. Watts, M. R. & Haus, H. A. Integrated mode-evolution-based polarization rotators. *Opt. Lett.* **30**, 138–140 (2005).

3. Schumann, M., Bückmann, T., Gruhler, N., Wegener, M. & Pernice, W. Hybrid 2D–3D optical devices for integrated optics by direct laser writing. *Light Sci. Appl.* **3**, e175 (2014).

4. Müller, P. *et al.* STED-inspired laser lithography based on photoswitchable spirothiopyran moieties. *Chem. Mater.* **31**, 1966–1972 (2019).

5. Heffner, B. L. Deterministic, analytically complete measurement of polarization-dependent transmission through optical devices. *IEEE Photon. Technol. Lett.* **4**, 451–454 (1992).

6. Bass, M & Mahajan, V. N. (Eds.) *Handbook of Optics, Third Edition, Volume I.* (McGraw-Hill, 2010).

7. Saleh, B. E. A. & Teich, M. C. *Fundamentals of Photonics*. (Wiley Interscience, 2007).

8. Mukherjee, B., Tomkos, I., Tornatore, M., Winzer P. & Zhao, Y. (Eds.) *Springer Handbook of Optical Networks*. (Springer Nature Switzerland AG 2020).

9. Raybon, G. *et al.* All-ETDM 80-Gbaud (640-Gb/s) PDM 16-QAM generation and coherent detection. *IEEE Photon. Technol. Lett.* **24**, 1328–1330 (2012).

10. Fatadin, I., Ives, D. & Savory, S. J. Blind equalization and carrier phase recovery in a 16-QAM optical coherent system. *J. Lightwave Technol.* **27**, 3042–3049 (2009).

11. Verbist, J. *et al*. A 40-GBd QPSK/16-QAM integrated silicon coherent receiver. IEEE Photonics Technology Letters **28**, 2070–2073 (2016).